SANDIA REPORT

SAND97–3092 • UC–405
Unlimited Release
Printed December 1997

Massively Parallel Computation of 3D Flow and Reactions in Chemical Vapor Deposition Reactors

Andrew G. Salinger, John N. Shadid, Scott A. Hutchinson, Gary L. Hennigan, Karen D. Devine, Harry K. Moffat

Prepared by
Sandia National Laboratories
Albuquerque, New Mexico 87185 and Livermore, California 94550

Sandia is a multiprogram laboratory operated by Sandia Corporation, a Lockheed Martin Company, for the United States Department of Energy under Contract DE-AC04-94AL85000.

Sandia National Laboratories

1. Introduction

Computer modeling of Chemical Vapor Deposition (CVD) reactors can greatly aid in the understanding, design, and optimization of these complex systems. Modeling is particularly attractive in these systems since the costs of experimentally evaluating many design alternatives can be prohibitively expensive, time consuming, and even dangerous, when working with toxic chemicals like Arsine (AsH_3): until now, predictive modeling has not been possible for most systems since the behavior is three-dimensional and governed by complex reaction mechanisms. In addition, CVD reactors often exhibit large thermal gradients, large changes in physical properties over regions of the domain, and significant thermal diffusion for gas mixtures with widely varying molecular weights. As a result, significant simplifications in the models have been made which erode the accuracy of the models' predictions. In this paper, we will demonstrate how the vast computational resources of massively parallel computers can be exploited to make possible the analysis of models that include coupled fluid flow and detailed chemistry in three-dimensional domains.

For the most part, models have either simplified the reaction mechanisms and concentrated on the fluid flow, or have simplified the fluid flow and concentrated on rigorous reactions. An important CVD research thrust has been in detailed modeling of fluid flow and heat transfer in the reactor vessel, treating transport and reaction of chemical species either very simply or as a totally decoupled problem. For instance, a good understanding of the behavior of a vertical rotating disk reactor has been gained through fluid flow and heat transfer models that take advantage of the axisymmetry of the reactor to reduce the problem to two spatial dimensions [6,7]. Using the analogy between heat transfer and mass transfer, and the fact that deposition is often diffusion limited, much can be learned from these calculations; however, the effects of thermal diffusion, the change in physical properties with composition, and the incorporation of surface reaction mechanisms are not included in this model, nor can transitions to three-dimensional flows be detected [8].

Two-dimensional models have also been used to analyze horizontal CVD reactors, by studying a cross-section of the reactor. Jansen *et al.* [9] and Ouazzani *et al.* [10] studied a horizontal CVD reactor with a tilted susceptor including a single transport equation for the limiting reactant, trimethylgallium (TMG). Unlike the rotating disk reactor, this configuration does not exhibit two-dimensional solutions, so the effects of disk rotation and side walls on the flow and heat transfer were neglected in their 2D model. Both papers did find that the Soret effect (thermal diffusion) could significantly change the predicted deposition rate.

In addition to the quest to compute 3D solutions, the other main CVD research thrust has been to incorporate detailed reaction mechanisms into reactor models that include transport effects. Due to the expense of rigorous treatment of the reaction chemistry, many of these models have been one-dimensional. Evans and Greif [11] presented a similarity solution for deposition on an infinite-radius rotating disk that reduces the three-dimensional Navier-Stokes equations to a one-dimensional model. This model was extended to include the transport equations by Coltrin *et al.* [12], a technology incorporated into the analysis code SPIN [13]. Since the infinite-disk idealized geometry approximates the rotating disk reactor, the similarity solution has been used to develop reaction mechanisms and kinetic parameters by fitting experimental data to the model predictions for the deposition of Silicon [14] and Gallium Arsenide ($GaAs$) [15]. Improved reaction mechanisms are continually being developed to model both gas phase and surface phase reactions. Examples for Gallium Arsenide deposition include a detailed mechanism by Masi *et al.* [16] with 17 gas phase species and a reduced mechanism by Moffat *et al.* [15] with 4 gas phase species with a surface blocking mechanism.

Our research effort is aimed at the synthesis of these two areas: reactor models with coupled 3D transport and detailed reaction mechanisms. Due to the large computational resources needed to tackle such a problem, there are few attempts in the literature. Ouazzani and Rosenberger [17] and Kleijn and Hoogendoorn [18] each solved three-dimensional models for reactant transport and GaAs deposition in horizontal reactors. The first paper decoupled the species transport from the fluid mechanics and heat transfer. Both works used solution procedures that require structured grids, so the effect of a rotating disk could not be readily included.

As will be discussed in detail in Section 2, considerable effort has gone into the development of the MPSalsa simulation code to make the CVD reactor model as accurate as possible. The diffusive flux of species includes a mixture averaged approximation and true multicomponent formulation with the effects of thermal diffusion included. All physical properties and reaction rates in the model are allowed to vary as functions of composition and temperature using the Chemkin [3] and Surface Chemkin [4] suites of library routines and the associated Tranlib [5] thermodynamic database. The geometry is discretized using an unstructured finite element mesh, which can flexibly represent complex geometries and features such as a rotating disk and allow increased mesh refinement in areas where steep gradients are expected.

The numerical methods, which are also discussed in Section 2, must be both fast and robust to form and solve the large set of discretized equations, and must be designed to run on a distributed memory architecture. It cannot be assumed that the entire mesh will fit on a single processor, so the mesh must be partitioned into hundreds or thousands of distinct domains, each to be loaded on a separate processor, in a way that the work load is balanced over all processors and that communications between processors is kept near a minimum. This domain decomposition is computed as a pre-processing step by the mesh-partitioning tool Chaco [19,20].

To solve the nonlinear coupled PDEs, a fully-coupled Newton's method is used. In our formulation the rows of the Jacobian matrix are stored fully summed. This storage uses considerably less memory than an element-by-element storage technique [21,22], and allows for the use of more sophisticated preconditioners for the iterative linear solution methods. To solve the resulting linear systems MPSalsa uses preconditioned Krylov methods as implemented in the Aztec iterative linear solver library [23], which has a number of iterative solution methods for linear systems, including GMRES [24], and domain-decomposition preconditioners.

These solution methods have high parallel efficiencies and have attained a peak speed of 210+GigaFLOPS (billions of floating point operations per second) on 7200 processors of the Sandia-Intel TFlop computer at Sandia National Labs for a reacting flow application [25]. In addition, the robust methodology has made it possible to directly reach steady-state solutions to many reacting flow problems from a trivial initial guess, including two of the three examples in this paper.

In Section 3 of this paper, we present results for three different reactor configurations that involve three-dimensional flows and chemical reactions. The first results are for a benchmark calculation, where we give evidence of the accuracy of our implementation by comparing a MPSalsa calculation with results from SPIN [13]. In the MPSalsa calculation, we solve the 3D problem for a disk of finite radius and examine solutions near the center of the disk. The second set of results is for the deposition of GaAs in a rotating disk reactor [6]. Our calculation is seen to match experimental results very well. The effect of the disk rotation rate on the rate and uniformity of the deposition shows the importance of this operating parameter on the success of the growth run. Transient calculations of the flow of non-reactive Helium through this reactor shows how transitions to unsteady, three-dimensional behavior can be predicted as well. The third set of results is a calcula-

tion for a reactor that admits only three-dimensional solutions. We use the CVD geometry of Jansen *et al.* [9] and model the deposition of GaAs in a horizontal channel reactor with tilted susceptor and rotating substrate. In this brief study the effect of rotation rate on the flow behavior and deposition rate uniformity is considered.

2. Model and Numerical Methods

2.1 Reacting Flow Model

In this section we discuss the governing equations for modeling reacting flow applications that are included in the MPSalsa computer code as well as MPSalsa's implementation of the finite element method for massively parallel computer architectures. Details of this implementation can be found in [1].

Table 1 shows the modeling equations implemented in MPSalsa that were used in this paper. The incompressible, variable density Navier-Stokes equations for laminar, Newtonian flow together with the continuity equation (with the anelstatic approximation) for total mass conservation govern the fluid flow. The heat balance includes contributions from convection, conduction, and reaction, but currently does not include terms coming from species interdiffusion, the Dufour effect, or radiative heat transfer. An arbitrary number of chemical species balances, with mass fractions as the primitive variables, include convection, diffusion, and reaction terms. The diffusive flux of each species contains terms from a non-dilute mixture-averaged diffusion formulation (a true multicomponent formulation is also available but has not been used for the results presented here) and for thermal diffusion (the Soret effect). We solve N_s -1 species balance equations with the last species equation replaced by the algebraic constraint that the mass fractions sum to unity.

Table 1. Governing Transport Equations for flow, heat transfer, and species transport and reaction. All physical properties vary with temperature and composition.

Momentum Balance:	$\rho\frac{\partial \mathbf{u}}{\partial t} + \rho(\mathbf{u}\cdot\nabla)\mathbf{u} = \nabla\cdot\sigma + \rho\mathbf{g}$, where $\sigma = -P\mathrm{I} + \mu(\nabla\mathbf{u} + \nabla\mathbf{u}^{\mathrm{T}}) - \frac{2}{3}\mu(\nabla\cdot\mathbf{u})\mathrm{I}$
Total Mass Balance:	$\nabla\cdot(\rho\mathbf{u}) = 0$
Thermal Energy Balance:	$\rho\hat{C}_p\frac{\partial T}{\partial t} + \rho\hat{C}_p(\mathbf{u}\cdot\nabla)T = \nabla\cdot\kappa\nabla T - \sum_{k=1}^{N_s} h_k W_k \dot{\omega}_k$
Mass Balance on Species k: $1 \le k \le N_s - 1$	$\rho\frac{\partial Y_k}{\partial t} + \rho(\mathbf{u}\cdot\nabla)Y_k = \nabla\cdot\left(\frac{\rho W_k}{\overline{W}} D_k \nabla X_k\right) + \nabla\cdot\left(D_k^T\frac{\nabla T}{T}\right) + W_k\dot{\omega}_k$
Mass Balance on Species N_s:	$\sum_{i=1}^{N_s} Y_i = 1$

For an accurate representation of reacting flows, all physical properties and reaction rates vary as a function of the local composition, local temperature, and thermodynamic pressure, which is assumed constant over the entire domain. This is done by linking with the Chemkin [3] and Surface Chemkin [4] libraries and the Tranlib [5] thermodynamic database. For reacting surfaces MPSalsa links with the Surface Chemkin library to model an arbitrary number of surface species and reactions. The surface site fractions on reacting surfaces are additional degrees of freedom in our solution. By using a pseudo steady approximation, which assumes that the time scale for the surface reactions is much faster than that for changes in the gas phase, the surface site fractions become an implicit function of the gas phase mass fractions and their calculation is decoupled from the gas-phase calculations. From the surface site fractions, the flux of the gas phase species is calculated to use as a boundary condition for the species balances. The sum of all these mass fluxes at any point on the surface gives the total mass flux into the surface, which is used as a boundary condition to specify the normal component of the velocity due to surface reaction -- often called the Stefan velocity. More details on this boundary condition and implementation are included in the following references [1,4,26].

The computations presented in this work are over three-dimensional domains and for mechanisms with up to 17 gas phase species, which leads to a model of up to 22 coupled nonlinear partial differential equations. The solution to these equations is approximated using a Petrov-Galerkin finite element method. All of the variables, $(\mathbf{u}, P, T, \mathbf{Y})$, are interpolated with trilinear basis functions within each hexahedral element of the unstructured mesh. A discrete set of residual equations is created by weighting each governing equation by each basis function and integrating over the domain. An additional pressure stabilization term is added to the continuity equation residual equations to allow for equal order interpolation of $\mathbf{u}$ and P [27,28]. The resulting discretized system consists of up to 10^6 equations and unknowns for the systems in this paper.

2.2 Numerical Methods

The MPSalsa reacting flows code has been developed to take advantage of the large speed and memory of distributed memory parallel computers so that models involving coupled 3D flows and detailed reaction mechanisms can be solved. Considerable investment was required in the development of parallel algorithms to solve for large problems on unstructured finite element meshes. It cannot be assumed that the entire mesh will fit on a single processor, so the mesh must be partitioned into hundreds or thousands of distinct domains, each to be loaded on a separate processor, and with each processor knowing which other processors it must communicate with to share information. An optimized graph-based partitioning algorithm (developed as an independent utility named CHACO [19,20]) is used to decompose an arbitrary unstructured finite element mesh into nearly equally-sized subdomains such that a minimum of communication is needed between the processors. This pre-processing utility runs on a single processor workstation, and requires only a few minutes to partition the meshes used in this paper. The impact of the quality of this partition on solution time is significant [29].

Since the transport equations are nonlinear, a robust solution procedure is used. A fully coupled Newton's method is used to solve the nonlinear problem, where all the equations are solved simultaneously, and all the interactions between the equations and variables are included in the Jacobian matrix. Each processor computes the residual equation and associated rows of the Jacobian matrix for the nodes it owns. Since these calculations are local, they exhibit near perfect scaling as the problem size and number of processors are increased proportionally [29]. In our implementation the matrix elements are fully summed. This method has the advantage of allowing a large set of

general algebraic preconditioners to be used. The ability to use robust preconditioning allows MPSalsa to often go directly to steady-state solutions for complex stiff problems. Fully summing the matrix rows also greatly reduces the operation count of the matrix-vector multiplication, which is the inner loop in most iterative matrix solvers [30], and significantly reduces the memory requirements for storing the matrix (over a stored matrix - element by element technique). In MPSalsa, the dependence of the physical properties on the solution is currently ignored in the Jacobian matrix for all properties except for the density and the reaction rate information. However many steady-state calculations still converge in $6 - 12$ Newton iterations.

At each iteration of the nonlinear solver, the linear system is solved iteratively using the Aztec library of preconditioned Krylov solvers. The computational core of these methods is a matrix-vector multiplication and the preconditioner, which dominates the cost of our entire solution procedure. In the calculations in this paper, we chose to first scale the matrix by a row-sum approach and use an incomplete LU decomposition as the preconditioner [31], a combination that we have found to be particularly robust. Then either the GMRES (Generalized Minimum Residual method [24]) or TFQMR (Transpose-Free Quasi-Minimal Residual method [32]) solver were used as the Krylov solver. For GMRES, a Krylov subspace size of $80 - 100$ vectors was used and restarted up to a maximum of 200–300 total iterations. When not enough memory was available on a given number of processors to store the Krylov subspace vectors, the TFQMR method was used with a limit of 400–600 total iterations.

We have a number of solution strategies in MPSalsa that form an outer loop around the nonlinear solver routine. In this paper we have used the simple steady-state solver and an implicit pseudo-transient calculation designed to reach steady-state quickly, which uses a forward-Euler, backward-Euler predictor-corrector scheme. There is also an accurate transient solution strategy with first and second order methods. For parametric and stability analysis studies, zeroth-order, first-order, and pseudo arc-length continuation strategies have been implemented.

An additional complexity in performing massively parallel computations is the I/O. MPSalsa has been used as the platform to develop Nemesis [34], a parallel I/O utility based on the Exodus [35] format for storing finite element meshes and solutions. Using Nemesis each processor writes its own output file to the parallel disk array, avoiding the bottleneck of hundreds of processors writing to a single file. From these files we have the capability of restarting calculations from old solutions as an initial condition for transient calculations or initial guesses for steady-state runs. At this time visualization and other post-processing still requires the solution to be stored in a single file.

3. Results and Discussion

In this section we present results of calculations made using MPSalsa on the Intel Paragon at Sandia National Laboratories. Three different three-dimensional reactor configurations were studied for the vapor phase deposition of Gallium Arsenide ($GaAs$) from a mixture of trimethylgallium ($GaMe_3$) and Arsine (AsH_2) in excess Hydrogen (H_2) carrier gas. Two different mechanisms for the gas and surface reactions of these compounds have been used in the following calculation: the blocking mechanism of Moffat *et al.* [15] which has 4 gas species, and a mechanism based on Masi *et al.* [16] that has 17 gas phase species.

The first calculations are for an idealized geometry -- flow impinging on a spinning disk of infinite radius -- for which there is a one-dimensional similarity solution that we use to benchmark our three-dimensional calculations. The second set of calculations are for the rotating disk reactor, for which we have experimental data to compare our computations against. The third set of calcula-

tions is for the horizontal CVD reactor with tilted susceptor, a geometry which admits no two-dimensional solutions. All three hexahedral finite element meshes were generated using the package CUBIT developed at Sandia [36].

In each section, a short discussion follows the presentation of the results.

3.1 The Infinite Disk Benchmark Problem

To establish the accuracy of our formulation and implementation, we have used both MPSalsa and the code SPIN [13] to calculate the deposition of GaAs in the idealized geometry of flow impinging on an infinite rotating disk. The SPIN program makes use of the von Karmen similarity solution for this configuration which reduces the problem to a one-dimensional system. Both codes use the same Chemkin, Surface Chemkin, and Tranlib libraries to calculate the reaction rates and physical and transport properties. The MPSalsa calculation is over a disk of finite radius and fully three-dimensional; however, solutions are compared near the center of the disk where edge effects are small.

The reaction mechanism of Masi, Simka, and Jensen [16] was used to model the gas and surface reactions of this system. We included the modification of Moffat *et al.* [15], where the sticking coefficient for $GaMe_3$ is dropped by two orders of magnitude. The mechanism consists of 17 gas phase species, 6 surface species, and 2 bulk solid species, and has 24 gas phase reactions and 37 surface reactions. Danckwerts' boundary condition [2] is used to specify the incoming mass flux of the species since the diffusive flux can not be ignored for this low pressure system.

The parameters at which the comparisons are made are shown in Table 2. Figure 1 shows the surface of the 3D finite element discretization used for the MPSalsa calculations, a discretization which leads to a problem size of one million unknowns. An ILU method with no overlap between processors with row-sum scaling of the matrix was used to precondition the linear system, which was solved using the TFQMR method. The job was run on 1824 compute nodes of the Intel Paragon at Sandia National Laboratories. An attempt to calculate the steady-state directly from a trivial solution did not succeed, so a transient scheme was used to relax the problem. Twenty time steps, with increasing step sizes starting from $\Delta t = 4.0 \times 10^{-5}$ were taken to reach a time of $t = 1$ second. From this solution, a jump to steady-state succeeded in 6 Newton iterations.

The total run required about 7 hours of compute time, with each fill of the Jacobian matrix and residual vector requiring about 40 seconds, and each linear solve, including preconditioning, requiring between 30 and 200 seconds, depending on the number of TFQMR steps taken. Most time steps took 4-5 Newton iterations to converge.

A visualization of the flow at the steady-state solution is shown in Figure 2. The reacting and spinning disk is colored black. Streamlines show an axisymmetric flow solution, with flow entering the top and leaving the sides.

Figure 3 compares the MPSalsa and SPIN solutions, by plotting 8 of the 22 variables as a function of the distance above the disk: the temperature, the three velocity components, and the mole fractions of 4 different species. The MPSalsa profiles are along a vertical line at radius $r = 1$. The species mole fractions are in excellent agreement between the two codes -- even for trace intermediate species such as AsHMe -- not only throughout the gas phase but at the reacting disk surface as well.

The agreement between the MPSalsa and SPIN calculations presented in Figure 3 verify the accuracy of our methodology and implementation. This includes the parallel aspects of the finite element method, the nonlinear solution method, and the linear solver, as well as the following phenomena: three-dimensional fluid mechanics, heat transfer, mass transfer with variable properties and thermal diffusion, gas phase reactions, surface reactions, and the Danckwerts' boundary condition. Even though the solution is axisymmetric, the MPSalsa calculation is truly 3D since it uses a Cartesian coordinate system and a non-axisymmetric mesh.

3.2 The Rotating Disk CVD Reactor

The rotating disk reactor is designed to take advantage of the perfect theoretical uniformity of the infinite disk configuration [8,6]. Figure 4 shows the geometry of this reactor, which consists of a cylindrical can placed concentrically within a larger cylindrical reactor. The main flow direction is axial, perpendicular to the top of the inner cylinder, which is the reacting surface. Spinning the inner cylinder, including the reactive disk, creates flow fields similar to the theoretical solution for the infinite disk configuration over much of the disk. The flow exits through the annular region between the two cylinders.

3.2.1 Steady-State Deposition of GaAs

The finite element mesh on two cross sections of the domain is shown in Figure 4. The details of the geometry, mesh, and parameters are given in Table 3. A reduced mechanism for the deposition of GaAs developed by Moffat *et al.* [15] -- which includes 4 gas phase species, 3 surface species, no gas phase reactions, and 3 surface reactions -- was used in these calculations. This reaction model includes a surface blocking effect of surface AsH_2, and fits deposition rate data well for a range of inlet feed rates. With this mechanism, the reactor model consists of 9 coupled PDEs.

A steady-state calculation for the system of 438,147 degrees of freedom requires 10 minutes on 300 processors of the Intel Paragon at Sandia National Labs. An ILU decomposition with no overlap between processors, with row-sum scaling is used as the preconditioner. Calculations with the block-Jacobi preconditioner -- which is simpler to implement and requires much less memory -- failed to converge to the steady-state without following a transient. The preconditioned linear system was solved by a restarted GMRES method, with a Krylov subspace dimension of 150 vectors, and a maximum of one restart per linear solve. The linear solver returned successfully when the residual was dropped by a factor of 5×10^{-4}.

Instantaneous contours of GaAs deposition in Angstroms/second are shown in Figure 5 for a disk spin rate of 300 rpm. At these conditions, the solution is axisymmetric. Even though deposition occurs over the entire disk of radius 3.75cm, the seeded crystal only covers out to a radius of 2.54cm. As can be seen in this figure, the deposition rate becomes highly non-uniform near the edge of the disk where fresh reactants can diffuse from the flow that heads into the annular region without passing over the disk.

Figure 6 shows a comparison of a MPSalsa calculation with experimental data [15] and a SPIN calculation for the effect of disk spin rate on the GaAs deposition rate in the rotating disk reactor. The SPIN calculation is for an infinite radius disk. Both the codes match the experimental data well at high spin rates, but only MPSalsa matches the solution at low spin rates where wall effects become more important. Appropriate error bars on the experimental data show all data points intersecting the MPSalsa calculation. It should be mentioned that the kinetic parameters in the reaction model were fit using SPIN from data gathered at 1000 rpm, including the three data points

shown here at 1000 rpm.

Using a first-order continuation method, the MPSalsa calculation for Figure 6 required about 2 hours on 300 processors of the Intel Paragon. Examination of the solutions showed that axisymmetric, steady-state solutions exist all the way down to zero spin rate at these values, although we have observed three-dimensional, unsteady solutions at other parameter values.

The results presented in Figure 6 for the rotating disk reactor show how the growth rate dependence on spin rate is captured by the MPSalsa calculation, even at low spin rates. We were expecting that the failure of the SPIN calculation to capture the behavior at low disk rotation rates was due to three-dimensional, time-dependent behavior, but axisymmetric steady-state solutions persisted to zero spin rate for this low density flow. Instead, it is the development of a parabolic flow profile, with velocities in the center of the reactor increasing above the plug flow inlet velocity, that is mainly responsible for the increase in the deposition rate above the SPIN prediction. Other runs, not shown here, have shown that the temperature of the wall can have a large effect on the deposition rates at low spin rates, presumably by effecting the temperature-dependent properties such as the viscosity and diffusion coefficients, as well as through the thermal diffusion mechanism (a.k.a. the Soret effect). The SPIN solution does match the deposition rate very well for a wide range of rotation rates. It can not, however, predict any radial variation in the growth rate.

The uniformity of the growth rate over the reacting surface as a function of the distance from the center of the disk can be calculated by averaging the instantaneous deposition rate over the azimuthal direction. (The averaging is trivial for these solutions since the deposition rate is already axisymmetric.) Figure 7 shows the deposition rate profiles over the disk for 5 different spin rates. The large edge effects are evident in all cases. The uniformity of the deposition over the seeded crystal varies from less than 1% at $\Omega = 1000$ to 15% at $\Omega = 0$. Even though the growth rate is higher at $\Omega = 1300$, $\Omega = 1000$ is a preferable operating condition because the growth is more uniform, and uniformity can be linked to the quality of the electronic devices made from the crystal. The matching condition for the given inlet flow rate (i.e., the spin rate of an infinite disk which would naturally pump the flow at this rate) is 1000 rpm.

The study of the effect of spin rate on deposition uniformity in the rotating disk reactor, Figure 7, shows a transition from concave deposition profiles at the center of the disk at low spin rates to a convex shape at $\Omega = 1300$, and the flattest profile near $\Omega = 1000$. The result that the most uniform growth in the rotating disk reactor occurs around $\Omega = 1000$ was expected since this spin rate is the matching condition for our flow rate.

3.2.2 Transient Fluid Flow and Heat Transfer

The calculations presented here were motivated by the experimental studies of Breiland and Evans [8], who investigated the conditions where the steady, axisymmetric flows in the rotating disk reactor become unstable. In this section, we present one transient calculation for the flow of Helium gas through the rotating disk reactor, at conditions where transient, fully three-dimensional solutions have been measured by Breiland [37].

The geometry and conditions of the run are described in Table 4. The geometry for this calculation is exactly the same as that in the previous section, as shown in Figure 4, and is discretized with a slightly finer mesh. The physical properties in the momentum, total mass, and heat transfer equations are calculated using Chemkin to be those for pure Helium at 626 torr and are dependent on the local temperature.

The problem was solved on 512 processors of the Intel Paragon at Sandia National Labs. A fully-implicit, first-order, time integration scheme (forward-Euler predictor, backward-Euler corrector) was used. The time step was adjusted based on a given error criterion using the method of Gresho et al. [38]. Because the variability of the physical properties was not included in the Jacobian (a.k.a. stiffness) matrix, a typical time step required 8 Newton iterations to converge, which is higher than one would expect to see with a complete Jacobian. The calculation of the residual equations and Jacobian matrix at each Newton iteration required 5 seconds, and a typical matrix solution time was 10-12 seconds using the GMRES method with a block-ILU preconditioner and row-sum scaling. Overall, the average time step required 2.5 minutes.

The long-time behavior of this calculation is shown in Figure 8, which shows the temperature at the coordinates (3.8, 0.0, 2.5) and (0.0, 3.8, 2.5). The solution is stable and periodic. Temperature readings at (-3.8, 0.0, 2.5) and (0.0, -3.8, 2.5) show that the solution exhibits 180 degree symmetry, which means that the local solution vector X obeys the equation,

$$X(x, y, z) = X(-x, -y, z). \tag{1}$$

A comparison of the calculated period and amplitude of the temperature variations with thermocouple readings from three experiments [37] (one at the same conditions as the simulation, and two at similar conditions) is shown in Table 5. The simulation and experiments all showed unsteady solutions with uniform amplitudes and period. At other conditions, experiments predicted steady solutions and chaotic-appearing time histories. The amplitude of the oscillations in the simulation agree well with those observed in two of the experiments, and the period matches well with that seen in the third experiment. (The calculated period of 1.8sec is the time between peaks of a curve in Figure 8. The real period of the flow is double that, 3.6sec, but because it exhibits 180 degree symmetry, the temperature profile repeats every 1.8sec. This smaller number is the fair number to compare with experiments, since they calculated the period by the single thermocouple reading).

We are satisfied with the agreement between the predictions and measurements, considering the many sources of discrepancies between the two, including (1) the calculation assumes a plug flow inlet velocity, which only approximates the experimental system, and (2) there are two thermocouples distorting the flow in the experiment, which may be responsible for slowing down the rotation period. It is also likely that multiple long-time behaviors exist for reactors operated at the same conditions, so perhaps our simulation reached a different attractor than the experimental runs.

The periodic solution is visualized in Figure 9 which shows the $T = 330K$ iso-surface at time $t = 9.58\text{sec}$. The 180 degree symmetry of the solution is evident. The long-time predicted behavior is for this surface to rotate around the reactor every 3.6sec, which corresponds to a rate of 17rpm. It would be interesting to study the complex interactions of fluid flow and geometry that choose this rotation rate, which must bridge the non-rotating flow at the inlet and disk rotation rate of 300rpm.

This one simulation shows promise that three-dimensional calculations can be used to identify stable and unstable ranges of operating and design parameters. These predictions could be especially beneficial during redesign and scale-up of reactor vessels.

3.3 The Horizontal CVD Reactor with Tilted Susceptor

The horizontal reactor with tilted susceptor and rotating substrate admits only three-dimensional solutions. The reactor configuration is presented in Figure 10, along with surface elements of the 43,568 element mesh. Details of the geometry, mesh, and parameters are shown in Table 6. The reactants enter the reactor through the rectangular region on the left. The bottom of the reactor slopes up at a 9 degree angle, forcing the flow to accelerate. The outlet of the reactor has only one quarter the area of the inlet face. The rectangular susceptor has a disk inset into the middle of it, which spins to average out the deposition rate. Tilting the base of the reactor is designed to offset the decline in deposition rate down the length of the reactor due to reactant consumption by accelerating the flow and shrinking the boundary layer over the disk, thereby decreasing mass transfer resistance to the surface. The two refined bands in the mesh at the beginning and end of the susceptor were added to resolve steep gradients in the deposition rate in the direction of the flow.

The reduced mechanism of GaAs deposition by Moffat *et al.* [15] is again used to model the reactions. Steady-state solutions of 432225 unknowns were reached directly from a trivial initial guess in 18 minutes on 288 processors of the Intel Paragon, using the same preconditioner, scaling, and linear solver as the rotating disk reactor calculation above. Each loading of the residual vector and Jacobian matrix required only 18 seconds, while the solution of each linear matrix problem needed, on average, about 100 seconds.

A representative solution for flow and deposition in the horizontal reactor with tilted susceptor is shown in Figure 11, for an inlet velocity of $V = 30\,\text{cm/sec}$ and disk spin rate $\Omega = 500\,\text{rpm}$. Streamlines for fluid that enters near the base of the reactor show the effect of the counter-clockwise rotation of the disk -- one path illustrating how fluid can be entrained to make multiple passes over the disk. The shaded contours on the susceptor visualize the gas phase mass fraction of $GaMe_3$ approaching the deposition surface, which is nearly proportional to the deposition rate since this is the limiting reactant. The asymmetry of the contours, which corresponds to non-uniform growth, illustrates the effect of large rotation rates.

This effect is examined in Figure 12, which contains contour plots of instantaneous $GaAs$ deposition in Angstroms/sec at $V = 30$ cm/sec for three different spin rates: $\Omega = 50$, $\Omega = 250$, and $\Omega = 500$. The surface finite element discretization over the disk is also shown. The solutions at the two higher rotation rates clearly show how the spinning disk can skew the deposition; however, the $\Omega = 50$ solution does not exhibit noticeable asymmetry. Deposition rates show decreased deposition near the walls, which is due to the formation of a parabolic flow profile.

In Figure 13, the instantaneous deposition rates that are shown in the previous figure are azimuthally averaged to account for disk rotation. The calculation of instantaneous deposition rates is based on the assumption that the surface reactions occur much faster than the transport phenomena, and the averaging assumes that the time for the growth run is long compared to the rotation period. An increase in disk rotation rate is shown to make the deposition profile more non-uniform, from 7.0% at $\Omega = 50$ to 8.2% at $\Omega = 500$.

Useful information on operating the horizontal reactor with a tilted susceptor can be obtained from this limited set of results presented in Figure 12 and Figure 13. The distortion of the instantaneous deposition contours at high disk rotation rates, as seen in Figure 12, are seen in Figure 13 to have an adverse effect on the uniformity of the time-averaged deposition profile; therefore, the reactor should be operated at low disk spin rates. This is different from the rotating disk reactor, which has an optimal spin rate far from zero. The symmetry of the instantaneous contours at $\Omega = 50$ show that this constitutes a low spin rate. Since the time-averaging of the instantaneous deposition assumes that the total growth run is long compared to the period of disk revolution, higher spin

rates must be used for growth runs that last only a few seconds, and also during transients at the beginning and the end of the run.

At the operating parameters of these calculations, the non-uniformity of the deposition rate due to disk spin rate is minor compared to other factors, since the non-uniformity is still an unacceptable 7% at the lowest spin rate. Inspection of Figure 12(a) shows that a boundary-layer of lower deposition rates along the side walls reaches into the disk. We believe that this is an effect of the momentum boundary-layer formed by the drag of the side walls, since a lower flow velocity will have a decreased mass transport to the surface. The averaged deposition profiles show a marked decrease in deposition at larger radii. These results suggest operation and design improvements that would improve the uniformity of the deposition rate. An increase in the flow velocity would decrease the size of the boundary layers along the side walls, so that the region of decreased deposition would not reach the disk. A design alternative would be to move the side walls further from the center of the disk, which would also move the boundary layer away from the disk. Both of these alternatives would unfortunately result in an increase in raw materials usage.

We are performing calculations that attempt to locate the optimal operating conditions and design of this reactor [39]. First, an objective function must be defined that collapses the entire finite element solution into a single real number, one that rewards uniform growth and low materials usage. By parameterizing the mesh motion so that design quantities such as the reactor width can be continuously varied, the objective function is then a function of just a handful of parameters. Optimization algorithms are then used to navigate parameter space and to locate the optimal parameter values.

4. Conclusions

The MPSalsa massively parallel chemically reacting flows code has been developed to solve three-dimensional flows (at low Mach number) coupled with chemical reactions using an unstructured finite element method. Through the use of the Chemkin libraries, the gas phase reactions, surface reactions, transport properties, and physical properties are rigorously modeled. Efficient and robust parallel algorithms allow for rapid solution of large systems of equations.

Considerable effort has been made in our development to take advantage of the large computational speed available on distributed memory machines. These efforts include the mesh partitioning algorithm for load balancing, efficient inter-processor communication, and an optimized matrix-vector multiplication routine. This has led to a top computation speed of 210+ GigaFLOPS and near perfect scaling as the problem size and number of processors are increased proportionately [25,29].

But since the goal is to solve the complex nonlinear problems, decisions have been made in the development process that prioritize robustness as well as speed. All the sensitivities of each equation with respect to each variable are computed and stored in the Jacobian matrix. This fully-coupled approach is memory-intensive, yet can be solved with Newton's method for rapid convergence.

Perhaps the most important investment in robustness is the use of expensive -- in terms of memory and CPU time -- preconditioners to solve the linear matrix problem. We found for the problems investigated here that an ILU factorization, which requires enough memory for a copy of the entire Jacobian, was needed to reach steady-state solutions directly. Also, when using the GMRES iterative technique, the ability of the linear solver to reduce the linear residual was highly dependent on

the size of the Krylov subspace. It was not unusual to need to store over 100 search vectors -- each vector having the length of the number of unknowns in the problem -- to be able to converge to steady-states from trivial initial guesses. It was not possible to get directly to the steady-state solution without following a transient for the infinite-disk benchmark problem with these methods, which accounts for the disproportionately longer CPU time needed for this problem than the two smaller steady-state reactor problems.

Since steady-state solutions were achieved for our reactor models in about 15 minutes on a fraction of our machine, we have begun detailed analyses of these reactor models. This will not only include parametric studies, such as the continuation run displayed in Figure 6, but optimization studies over several parameters as well. Optimization of operating parameters, such as inlet flow rates and disk rotation rates, can aid operators in understanding the responses of the reactor to these parameters. Even more informative will be optimization studies that include design parameters, which can not be affordably studied experimentally. Current efforts include the study of an alternative inlet design of the rotating disk reactor to minimize raw materials costs while not sacrificing growth uniformity, and a variation of the tilt angle in the horizontal reactor with tilted susceptor. Without the investment in efficient and robust methods for parallel solutions, detailed analysis of these models would not be feasible.

References

1. J. N. Shadid, H. K. Moffat, S. A. Hutchinson, G. L. Hennigan, K. D. Devine, and A. G. Salinger, Sandia National Laboratories Technical Report, SAND95–2752 (1996).
2. A.G. Salinger, K.D. Devine, G.L. Hennigan, H.K. Moffat, S.A. Hutchinson, and J.N. Shadid, Sandia National Laboratories Technical Report, SAND96-2331 (1996).
3. R. J. Kee, F. M. Rupley, E. Meeks, and J. A. Miller, Sandia National Laboratories Technical Report, SAND96–8215 (1996).
4. M. E. Coltrin, R. J. Kee, and F. M. Rupley, E. Meeks, Sandia National Laboratories Technical Report, SAND96-8217 (1996).
5. R. J. Kee, G. Dixon-Lewis, J. Warnatz, M. E. Coltrin, J. A. Miller, Sandia National Laboratories Technical Report, SAND86–8246 (1986).
6. G. Evans and R. Greif, *J. Heat Transfer*, **109**, (1987) 928-935.
7. G. Evans and R. Greif, *Numer. Heat Transfer*, **12**, (1987) 243-252.
8. W. G. Breiland and G. H. Evans, *J. Electrochem Soc*, **138**(6), (1991) 1806-1816.
9. A.N. Jansen, M.E. Orazem, B.A. Fox, and W.A. Jesser, *J. Crystal Growth*, **112**, (1991) 316-336.
10. J. Ouazzani, K.-C. Chiu, and F. Rosenberger, *J. Crystal Growth*, **91**, (1988) 497-508.
11. G. Evans and R. Greif, *Numer Heat Transfer*, **14**, (1988) 373-387.
12. M. E. Coltrin, F. J. Kee, and G. H. Evans, *J. Elechtrochem. Soc.*, **136**(3), (1989) 819-829.
13. M. E. Coltrin, F. J. Kee, G. H. Evans, E. Meeks, F. M. Rupley, and J. F. Grcar, Sandia National Laboratories Technical Report, SAND87–8248 (1987).
14. P. Ho, M.E. Coltrin, and W.G. Breiland, *J. Phys. Chem.*, **98**(40), (1994) 10138-10147.
15. H. K. Moffat, K. P. Killeen, and K. C. Baucom, (1995) submitted.
16. M. Masi, H. Simka, and K.F. Jensen, *J. Crystal Growth*, **124**, (1992) 483-492.
17. J. Ouazzani and F. Rosenberger, *J. Crystal Growth*, **100**, (1990) 545-576.
18. C.R. Kleijn and C.J. Hoogendoorn, *Chem. Eng. Sci.*, **46**(1) (1991) 321-334.
19. B. Hendrickson and R. Leland. Proceedings of *Supercomputing '95*, ACM, November (1995).

20. B. Hendrickson and R. Leland, Sandia National Laboratories Technical Report, SAND94-2692 (1995).

21. A.G. Salinger, Q. Xiao, Y. Zhou, and J.J. Derby, *Comput. Methods Appl. Mech. Engng*, **119**, (1994) 139-156.

22. M. Behr, A. Johnson, J. Kennedy, S. Mittal, and T. Tezduyar, *Comput. Methods Appl. Mech. Engng*, **108**, (1993) 99-118.

23. S. A. Hutchinson, J. N. Shadid and R. S. Tuminaro, Sandia National Laboratories Technical Report, SAND95–1559 (1995).

24. Y. Saad and M.H. Schultz, *SIAM J. Sci. Stat. Conp.*, **7**(3), (1986) 856-859.

25. J. N. Shadid, S. A. Hutchinson, K. D. Devine, G. L. Hennigan, A. G. Salinger, R. S. Tuminaro, Proceedings of SC'97, San Jose, CA, (1997).

26. R. Venkataramani, H.K. Moffat, A.G. Salinger, (1996) in preparation.

27. T. J. R. Hughes, L. P. Franca, M. Balestra, *Comp. Meth. App. Mech. and Eng.*, **59**, (1986) 85–99.

28. T. E. Tezduyar, *Advances in App. Mech.*, **28**, (1992) 1–44.

29. J. N. Shadid, S. A. Hutchinson, G. L. Hennigan, H. K. Moffat, K. D. Devine, A. G. Salinger, *Parallel Computing* (1996) submitted.

30. J. N. Shadid and R. S. Tuminaro, *Concurrency: Practice and Experience*, **4**, (1992) 481-497.

31. J. A. Meijerink and H. A. van der Vorst, *J. Comput. Phys.*, **44**, (1981) 134-155.

32. R. W. Freund and N. M. Nachtigal, *Numer. Math.*, **60**, (1991) 315-339.

33. M.S. Eldred, W.E. Hart, W.J. Bohnhoff, V.J. Romero, S.A. Hutchinson, and A.G. Salinger, *Proceedings of the 6th AIAA/NASA/ISSMO Symposium on Multidisciplinary Analysis and Optimization,* AIAA-96-4164-CP, Bellevue, WA, (1996) 1568-1582.

34. G.L. Hennigan, J. N. Shadid and M. M. St. John, Sandia National Laboratories Technical Report, (1997) in preparation.

35. L. A. Schoof and V. R. Yarberry, Sandia National Laboratories Technical Report, SAND92–2137 (1994).

36. T. D. Blacker *et al.*, Sandia National Laboratories Technical Report, SAND94–1100, May (1994).

37. W. G. Breiland, (1996) private communication.

38. P.M. Gresho, R.L. Lee, and R.L. Sani, Recent Advances in Numerical Methods in Fluids, Vol. 1, Pineridge Press, Swansea, U.K., (1980) 27-81.

39. A. G. Salinger, J.N. Shadid, H.K. Moffat, S.A. Hutchinson, G.L. Hennigan, K.D. Devine, and W.E. Hart, (1997) in preparation.

Table 2. Parameters for MPSalsa and SPIN calculations of GaAs deposition via flow impinging on a rotating disk.

Height of inlet above disk	10 cm	Pressure	70 torr
Radius of disk (MPSalsa only)	7.00 cm	GaAs mechanism	[16]
Rotation rate of disk, Ω	30 rpm	Number of unknowns per node	22
Inlet flow rate, V	10 cm/sec	Number of Elements (MPSalsa)	41,819
Inlet mole fraction: ($GaMe_3$)	0.000135	Number of nodes (SPIN)	229
Inlet mole fraction: (AsH_2)	0.004395	Number of nodes (MPSalsa)	45,504
Inlet mole fraction: (H_2)	0.995470	Number of unknowns (SPIN)	5,038
Inlet gas temperature	300K	Number of unknowns (MPSalsa)	1,001,088
Disk temperature	913K		

Table 3. Parameters for MPSalsa calculations for GaAs deposition in the vertical rotating disk reactor.

Height of inlet above disk	10 cm	Wall temperature	293K
Radius of reactor	5.75 cm	Disk temperature	913K
Radius of reacting surface	3.81 cm	Pressure	70 torr
Rotation rate of disk, Ω	0--1500 rpm	GaAs mechanism	[15]
Inlet flow rate, V	29.15 cm/sec	Number of unknowns per node	9
Inlet mole fraction: ($GaMe_3$)	0.000135	Number of Trilinear Elements	45,580
Inlet mole fraction: (AsH_2)	0.004395	Number of nodes	48,683
Inlet mole fraction: (H_2)	0.995470	Number of unknowns	438,147
Inlet gas temperature	303K		

Table 4. Parameters for MPSalsa calculations for He flow in the vertical rotating disk reactor.

Height of inlet above disk	10 cm	Wall temperature	295K
Radius of reactor	5.75 cm	Disk temperature	600K
Radius of reacting surface	3.81 cm	Pressure	626 torr
Rotation rate of disk, Ω	300 rpm	Number of unknowns per node	5
Inlet flow rate, V	0.51 cm/sec	Number of Trilinear Elements	47,004
Inlet mole fraction: He	1.00	Number of nodes	50,202
Inlet gas temperature	295K	Number of unknowns	251,010

Table 5. Comparison of the calculated transient temperature behavior with three experimental results at the same or similar conditions.

Source	Inlet Velocity	Period	Amplitude
Present Calculation	0.51 cm/sec	1.8 sec	38C, uniform
Experiment [37]	0.51 cm/sec	8 sec	50 C, uniform
Experiment [37]	0.48 cm/sec	8 sec	45 C, uniform
Experiment [37]	0.46 cm/sec	2 sec	10 C, uniform

Table 6. Parameters for the MPSalsa calculation of GaAs deposition in the horizontal reactor with tilted susceptor.

Reactor Length	22.0 cm	Inlet mole fraction: (H_2)	0.995470
Reactor Length Before Tilt	3.0 cm	Inlet gas temperature	298K
Susceptor Length	10.0 cm	Top Wall temperature	675K
Reactor Height at Inlet	4.0 cm	Susceptor and Disk temperature	913K
Reactor Width	9.0 cm	Pressure	70 torr
Tilt Angle	9 degrees	GaAs mechanism	[15]
Disk Radius	3.5 cm	Number of unknowns per node	9
Disk Rotation Rate, Ω	50-500 rpm	Number of Trilinear Elements	43,568
Inlet Flow Rate, V	30 cm/sec	Number of nodes	48,025
Inlet mole fraction: ($GaMe_3$)	0.000135	Number of unknowns	432,225
Inlet mole fraction: (AsH_2)	0.004395		

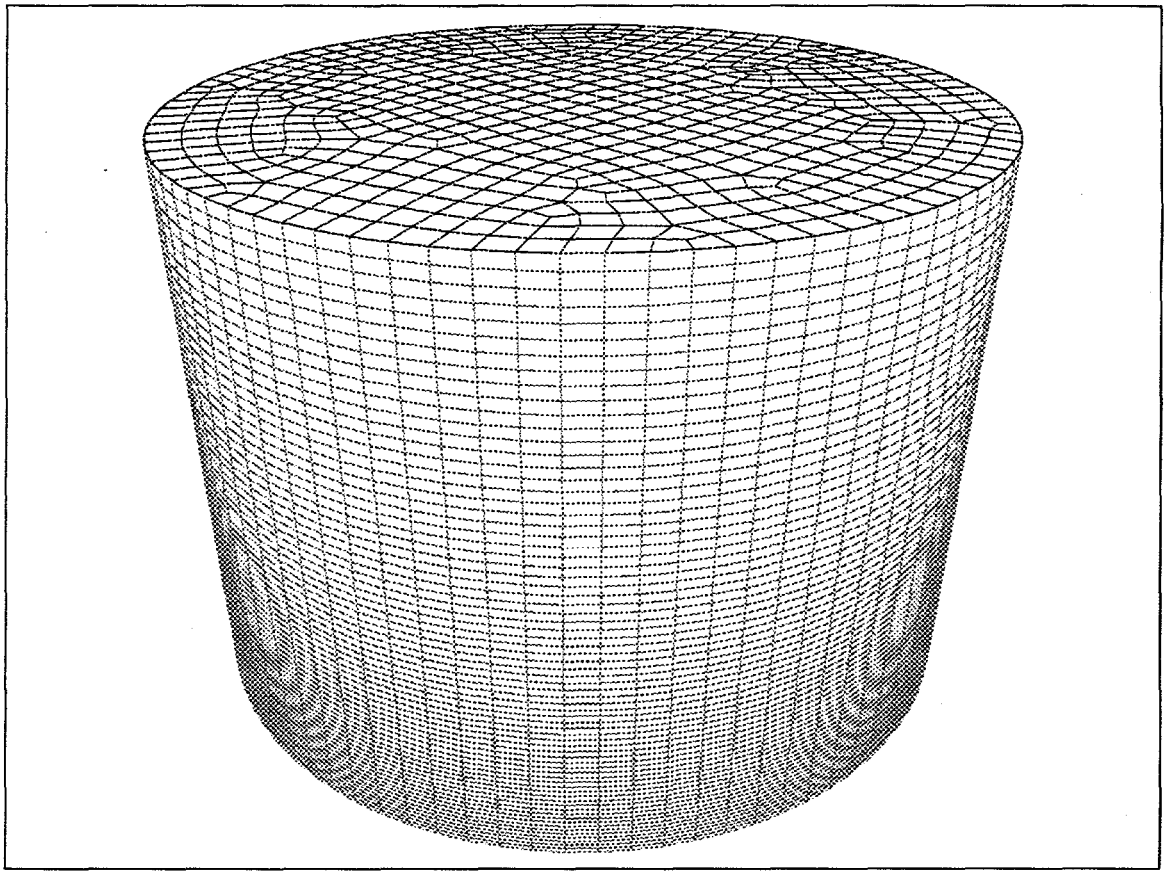

Figure 1. Surface elements of the mesh used for the comparison of MPSalsa and SPIN, which solves for reacting flows impinging on a disk of infinite radius. The reactants enter the top circular boundary of the domain, and react on a heated, spinning disk at the bottom of the domain. This mesh has 45,504 nodes which corresponds to a problem with 1,001,088 degrees of freedom, as shown in Table 2.

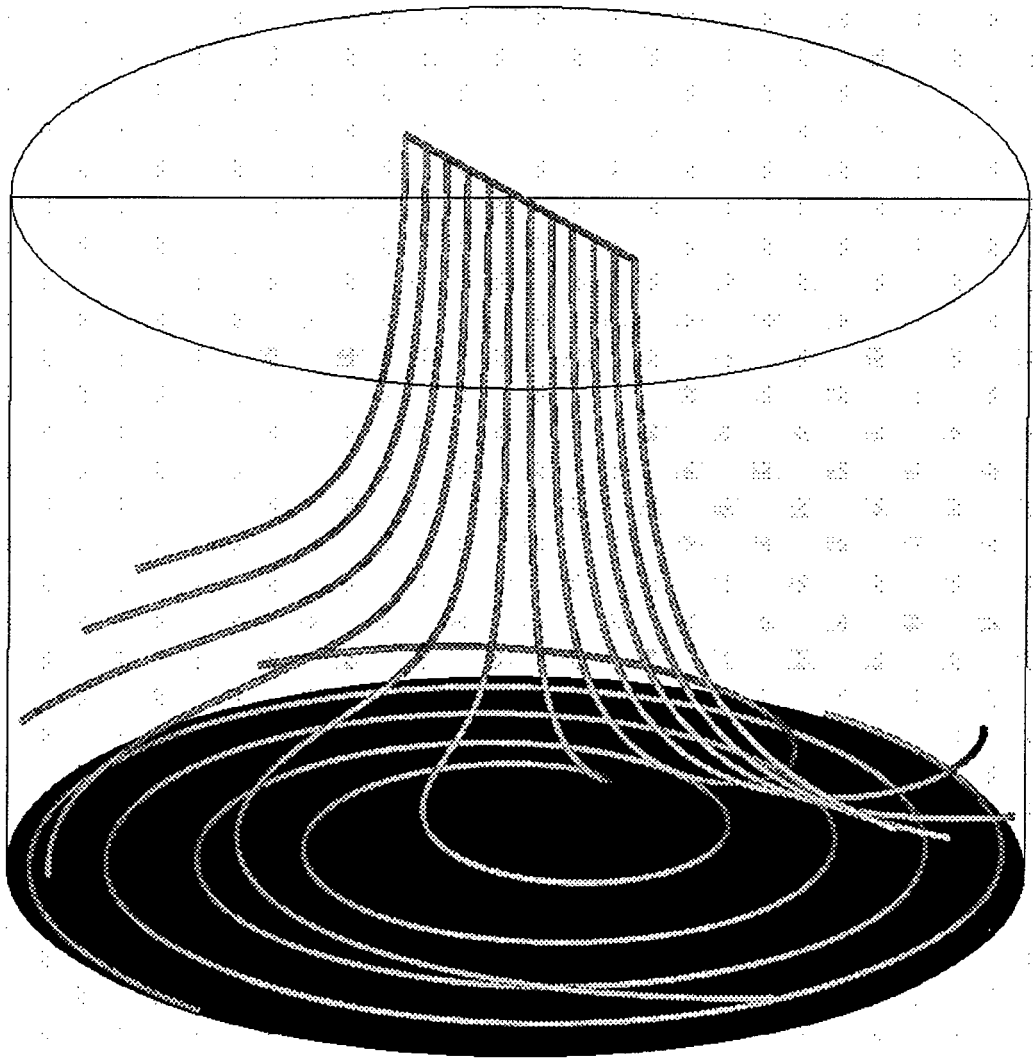

Figure 2. Streamlines for the MPSalsa calculation of flow impinging on a rotating disk. The lower disk is rotating at 30 rpm. The details of the calculation are shown in Table 2.

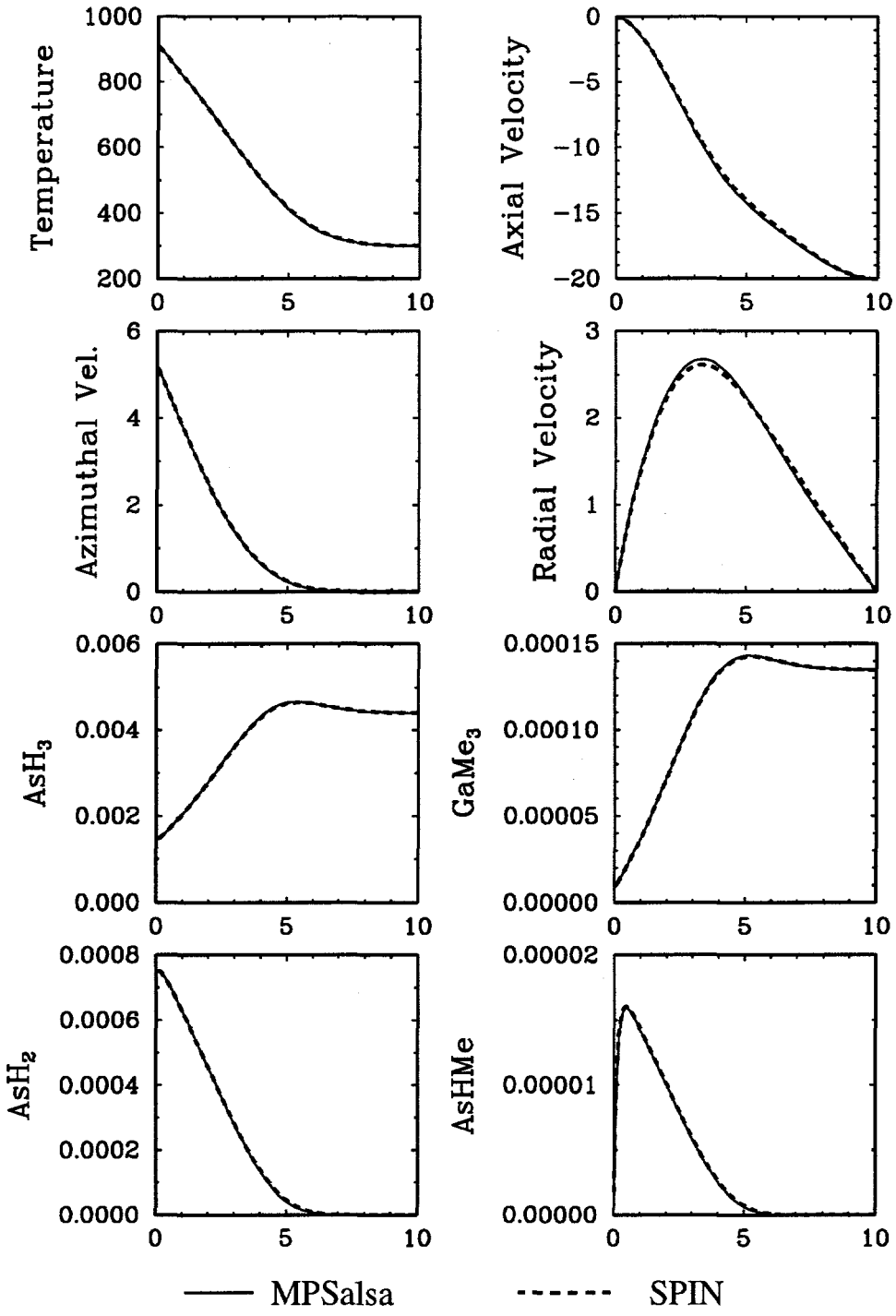

Figure 3. A comparison of MPSalsa and SPIN for flow impinging on a rotating disk. The SPIN code assumes that the disk has infinite radius, while the geometry of the MPSalsa calculation is described in Table 2 and shown in Figure 1. The MPSalsa results are along a vertical line at a radius of 1 cm. The excellent agreement benchmarks the accuracy of nearly all parts of our reacting flows implementation, including surface and gas phase reactions, fluid flow, and heat and mass transfer. The temperature is in degrees K, the velocities have units of cm/sec, while the species plot mass fraction. The abscissa is the height above the disk in centimeters.

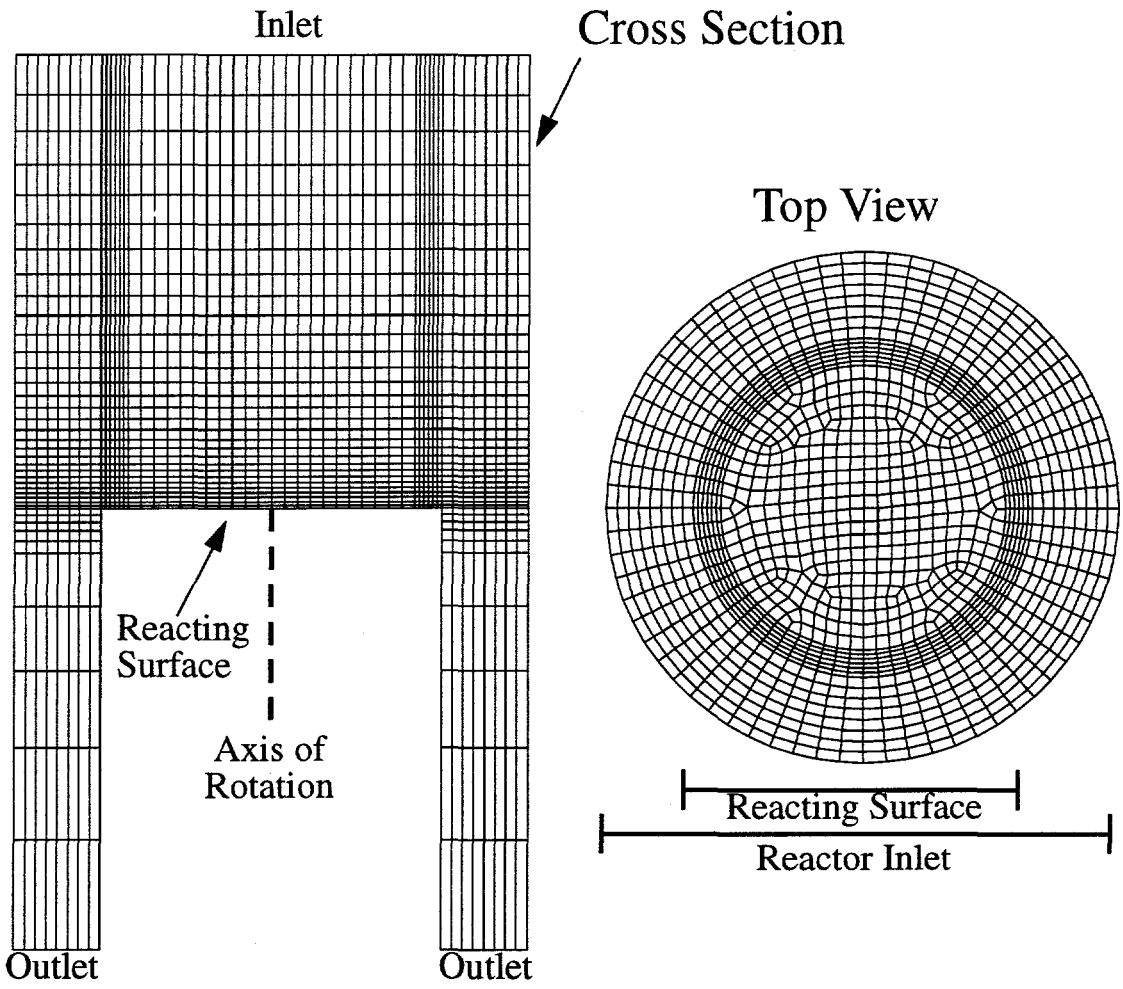

Figure 4. A cross section and top view of the rotating disk reactor geometry, showing the finite element mesh. The design consists of one cylinder inside a bigger one, with the reacting surface on the top of the inner cylinder, which is usually rotating. The flow enters uniformly within the entire top circle, flows over the disk, and flows out through an annular region. Details of the geometry and mesh are in Table 3.

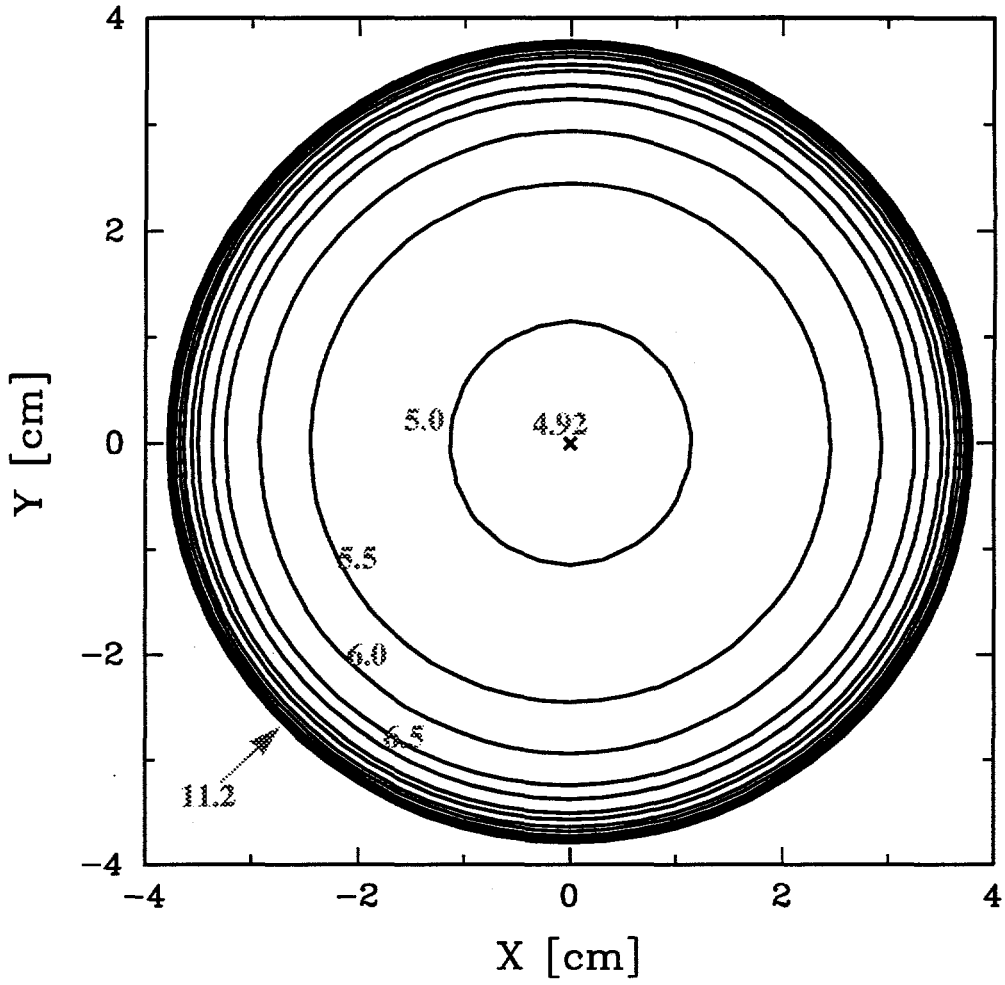

Figure 5. Instantaneous contours of GaAs deposition rate in the rotating disk reactor, labeled in units of Angstroms/sec, which show an axisymmetric growth profile. This is a steady-state solution at $\Omega = 300$ rpm, and details of the geometry, mesh, and other parameters are shown in Table 3. This three-dimensional calculation with 438,147 unknowns to a steady-state from a trivial initial guess required 10 minutes on 300 processors of the Intel Paragon at Sandia National Labs.

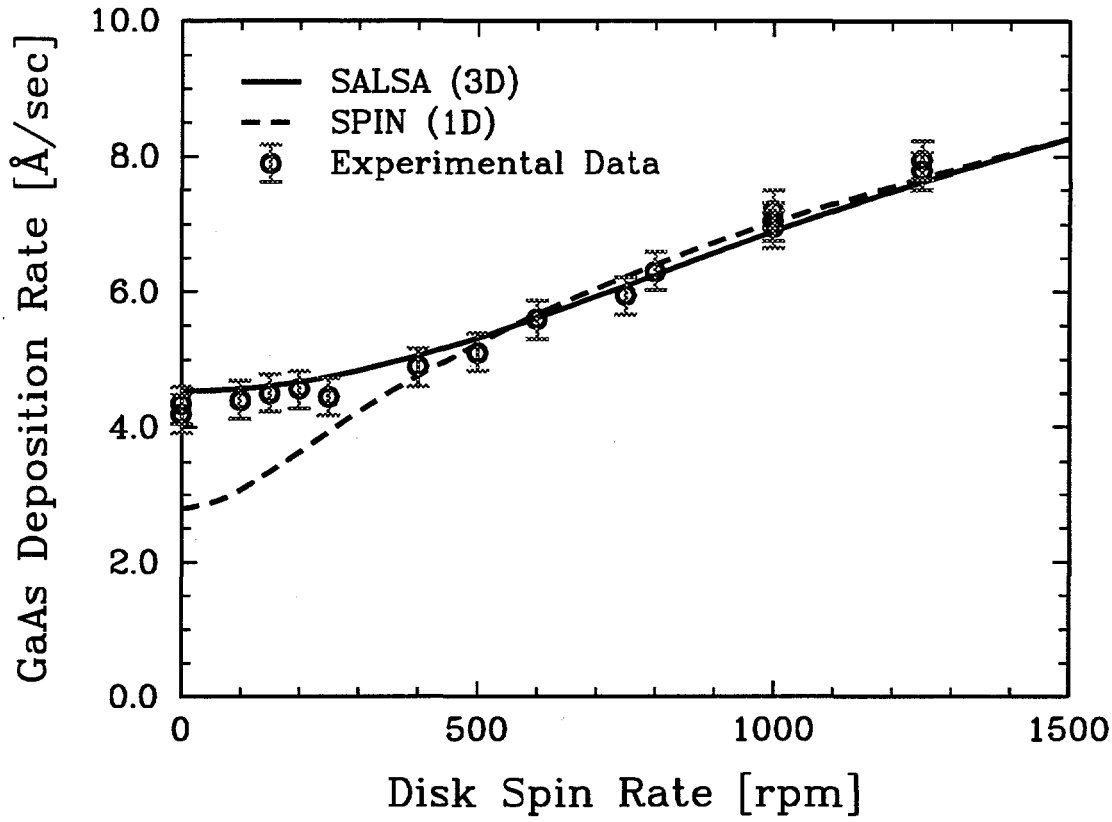

Figure 6. Comparison of MPSalsa, SPIN, and Experimental data [15] for the deposition rate at the center of the disk as a function of disk spin rate. See Table 3 for details of the geometry, mesh, and operating conditions. For low spin rates, the outer wall -- not captured by the SPIN model but included in the MPSalsa model -- significantly effects the deposition rate at the center. The kinetic parameters used in both calculations were fit using SPIN, using this and other experimental data, at 1000 rpm [15].

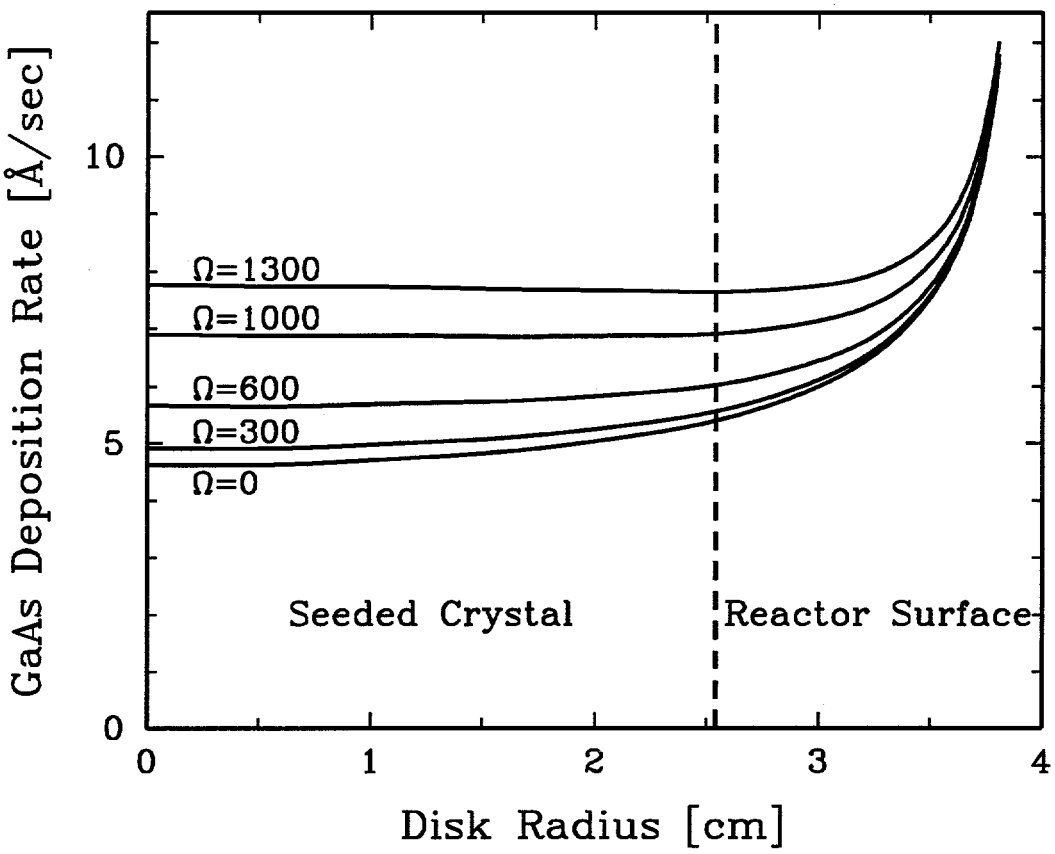

Figure 7. Time-averaged deposition rate profiles along the rotating disk reactor for a number of different rotation rates, Ω, in rpm. Even though deposition occurs over the entire surface, only the deposition on the seeded crystal is of practical interest. The uniformity of deposition over the seeded crystal ranges from a less than 1% deviation at $\Omega = 1000$ up to 15% at $\Omega = 0$.

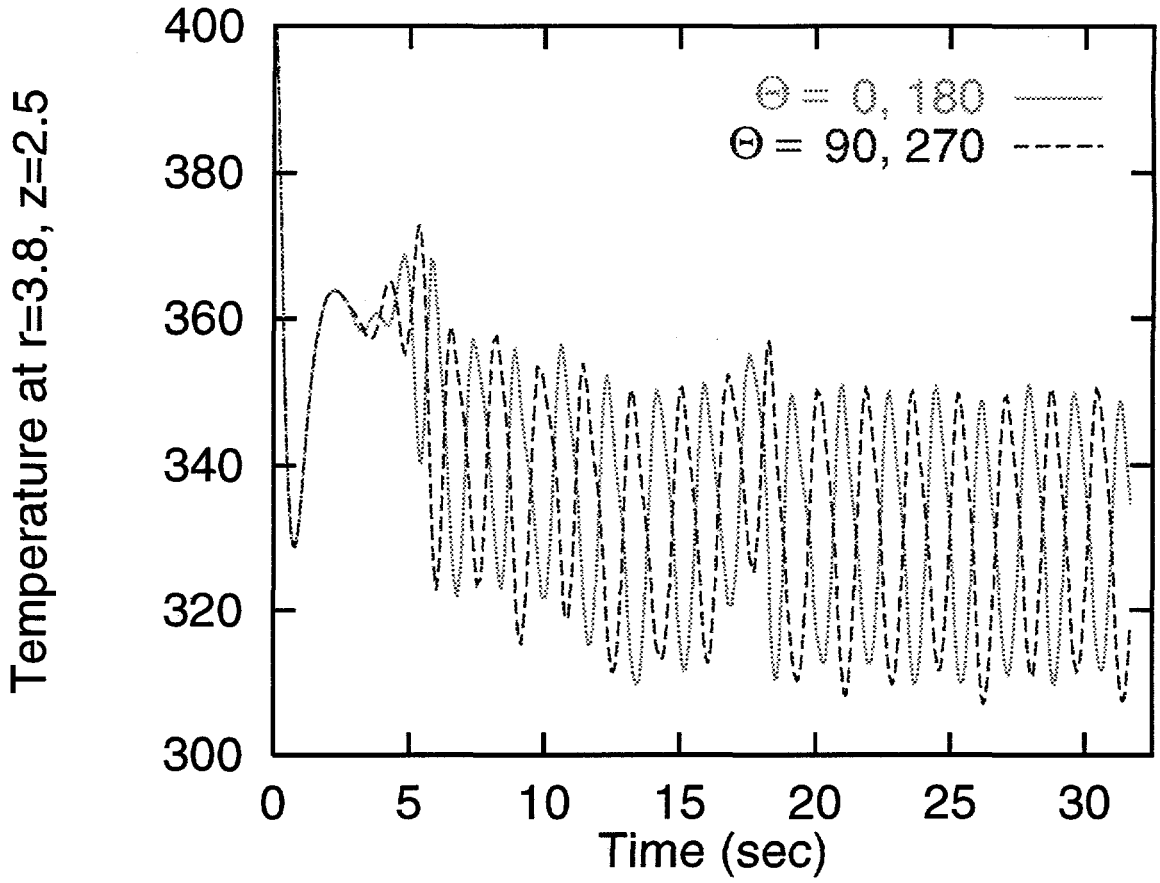

Figure 8. Temperature at four positions for a transient calculation of flow in the rotating disk reactor. The solutions at positions that are 180 degree angle apart coincide exactly while solutions at positions 90 degrees apart are directly out of phase, implying a period-2 solution. Conditions for this calculation are shown in Table 5.

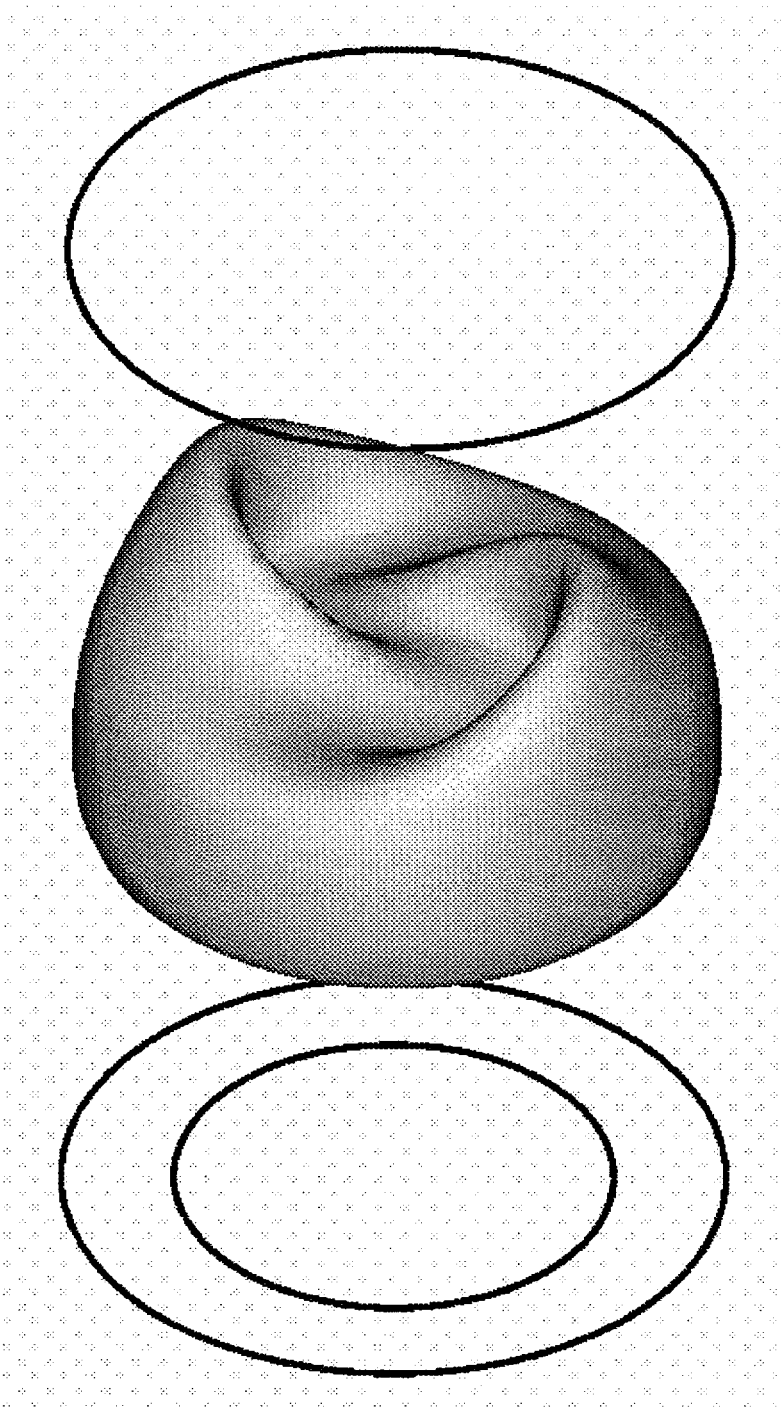

Figure 9. Iso-surface corresponding to $T = 330K$ at time $t = 9.58\text{sec}$ for the transient calculation of Helium flow in the rotating disk reactor. The two-fold (180 degree) symmetry is evident. The two peaks illustrate where the warm gas is being convected upward from the disk.

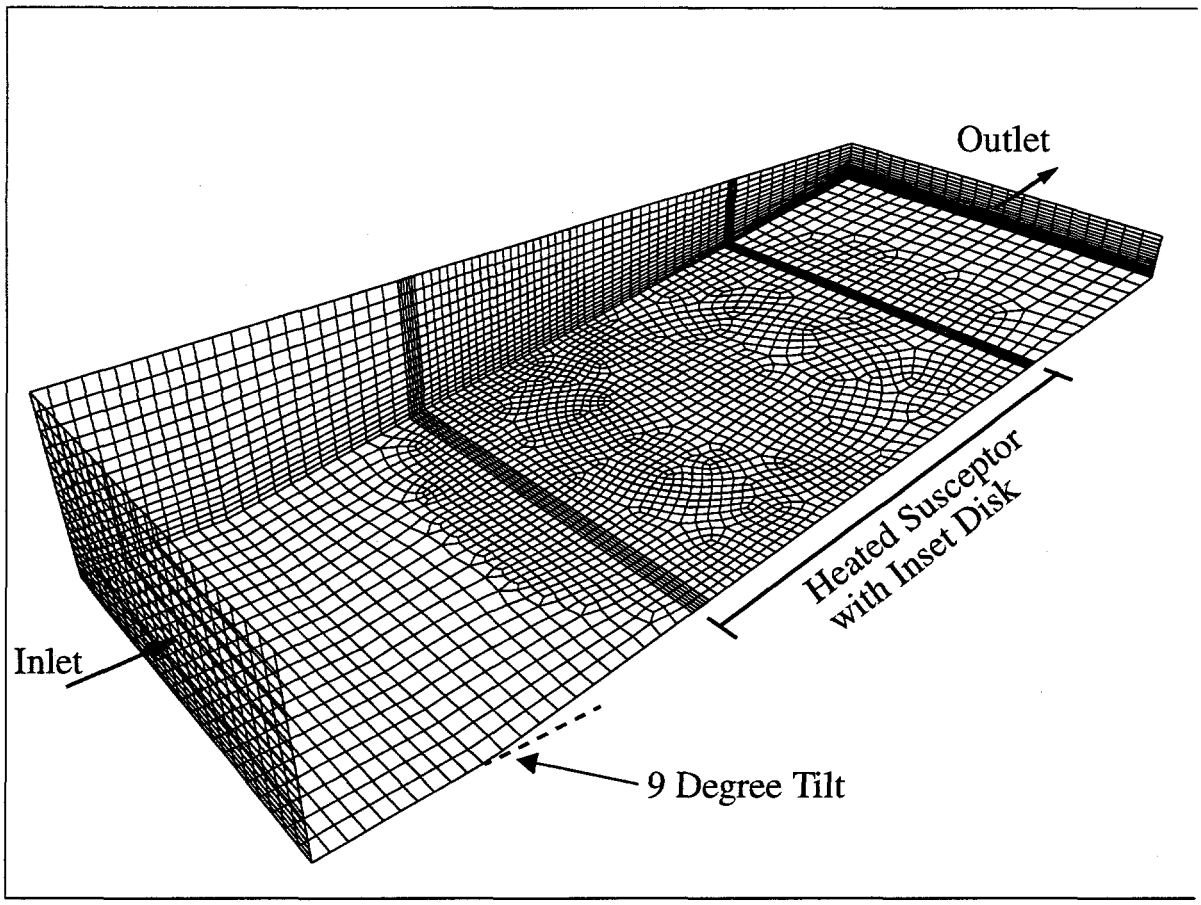

Figure 10. Surface elements of the mesh for the horizontal reactor with tilted susceptor. The details of the geometry and mesh are described in Table 6. Although deposition occurs over the entire rectangular susceptor area, the crystal is only seeded on the inset spinning disk. The 3D mesh contains of 48,025 nodes, which corresponds to 432,225 unknowns.

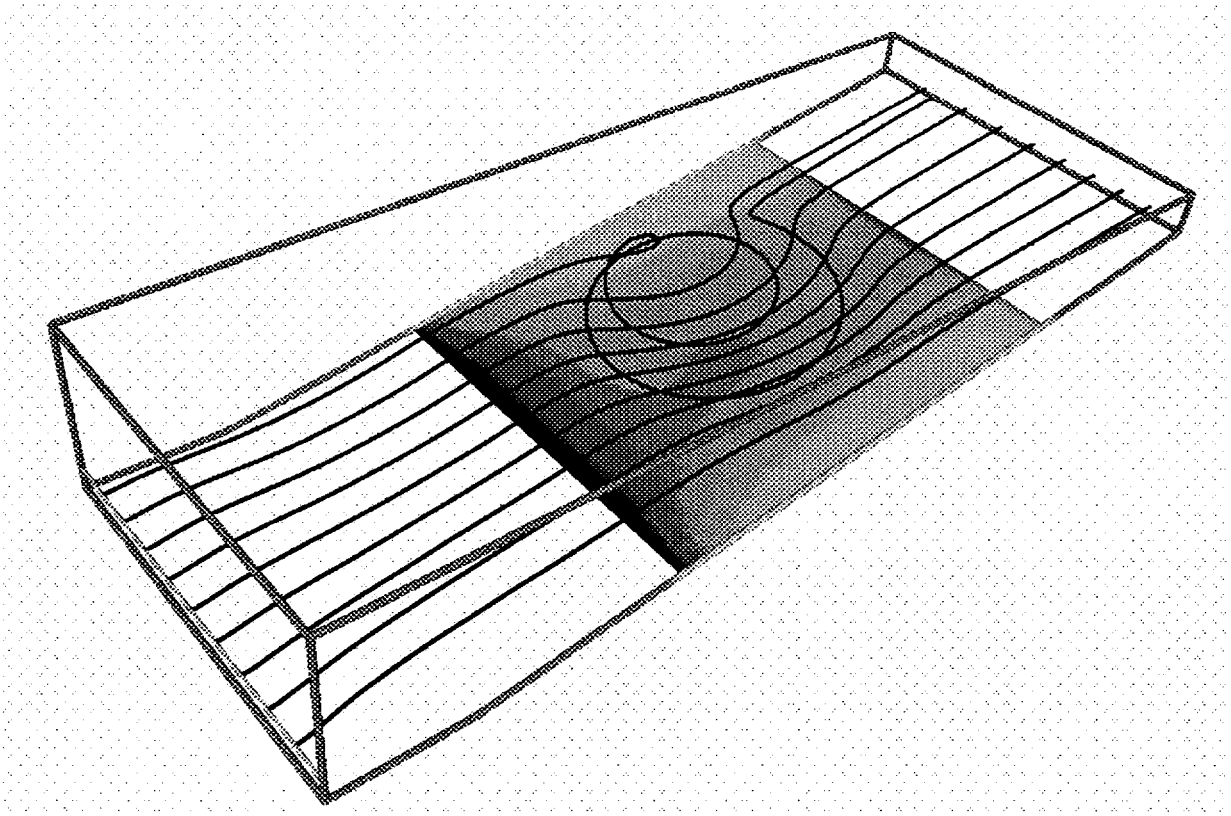

Figure 11. Visualization of a solution for $GaAs$ deposition in the horizontal CVD reactor with tilted susceptor, at rotation rate $\Omega = 500$ rpm and inlet velocity $V = 30$ cm/sec. See Table 6 for other information geometry, mesh, and parameters. Streamlines released near the bottom of the inlet surface show the effect of the spinning disk on the flow profile, including one path where the fluid gets entrained for multiple passes over the disk. The shaded contours on the susceptor show the mass fraction of the limiting reactant, $GaMe_3$, on the surface, which corresponds well with deposition rate. The asymmetry in the contours is due to the disk rotation.

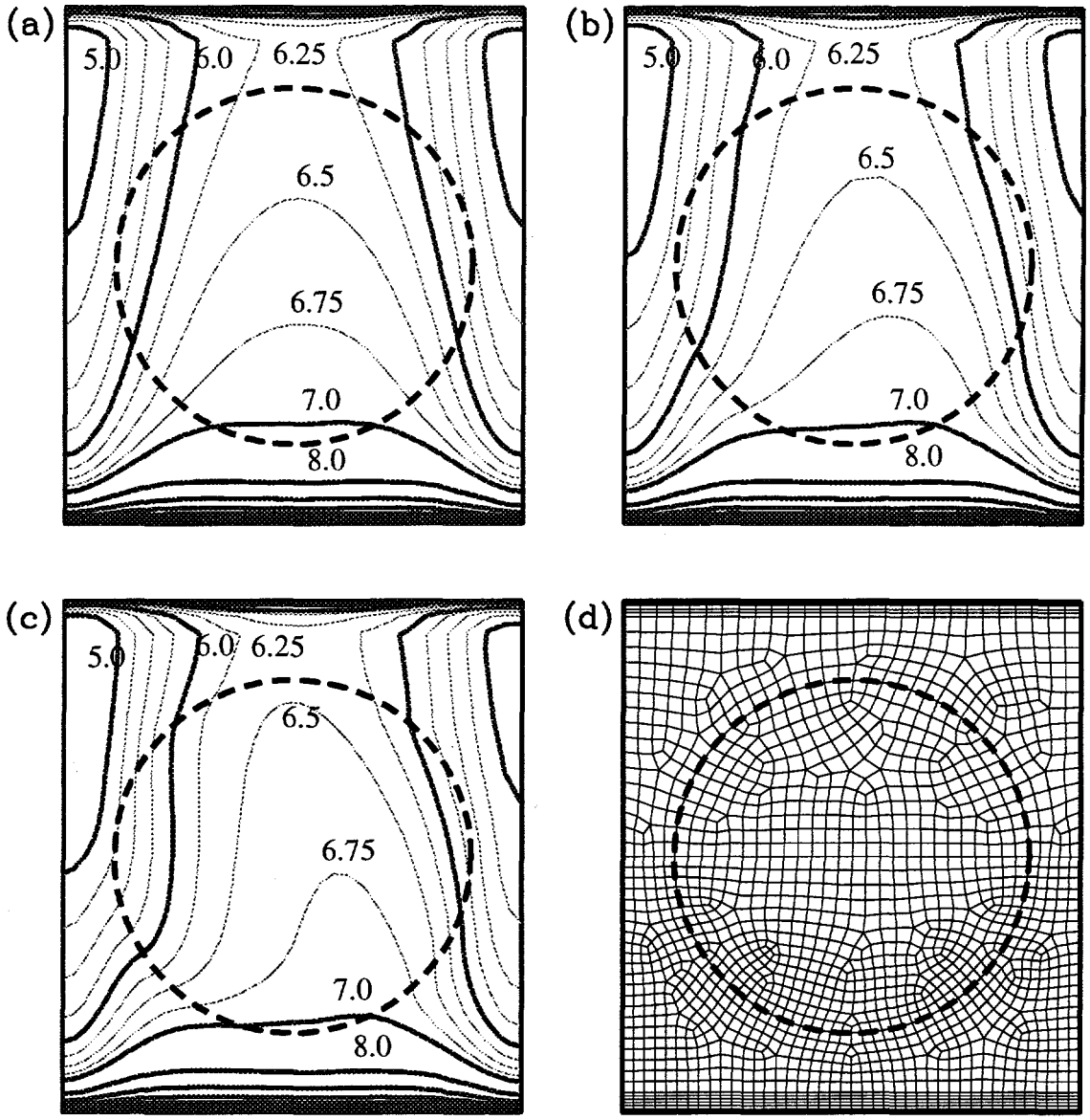

Figure 12. Instantaneous contours of GaAs deposition rates over the entire susceptor in Angstroms/ sec, (a)-(c), and the surface elements of the finite element discretization, (d). Deposition is only seeded in the center disk area, which spins. The main flow direction is up in these plots. The inlet velocity for all three contour plots is $V = 30$ cm/sec, with disk rotation rates (a) $\Omega = 50$, (b) $\Omega = 250$, and (c) $\Omega = 500$. The higher spin rates significantly deform the deposition rates from a symmetric solution.

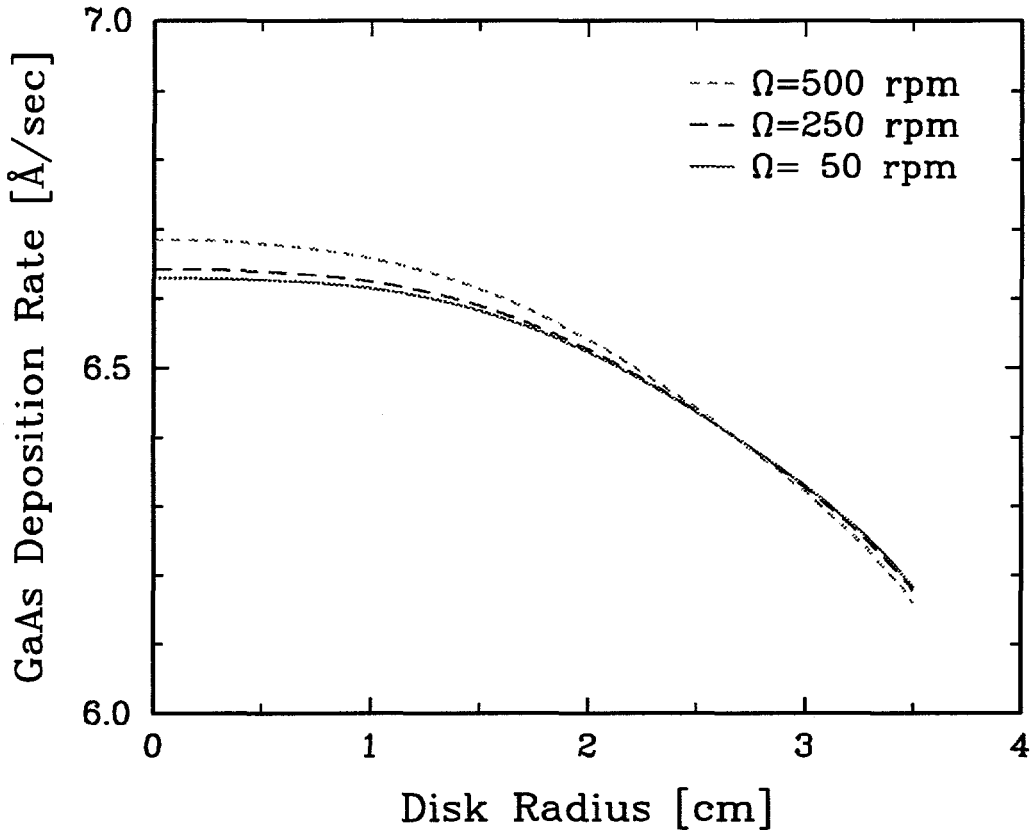

Figure 13. Time-averaged (i.e., azimuthally-averaged) GaAs deposition rates over the rotating disk in the horizontal CVD reactor with tilted susceptor, calculated by integrating out the Q component of the contours shown in the previous figure. The asymmetry caused by the higher disk rotation rates causes an increase in the non-uniformity of the averaged deposition rates, from 7.0% at $\Omega = 50$ to 8.2% at $\Omega = 500$.

EXTERNAL DISTRIBUTION:

Rich A. Cairncross
Department of Chemical Engineering
Drexel University
Philadelphia, PA 19104

G. F. Carey
ASE/EM Dept., WRW 305
University of Texas
Austin, TX, 78712

Vernon Cole
Equipment Simulation Group, APRDL
3501 Ed Bluestein Boulevard, MD: K-10
Austin, TX 78721

Dan Coronell
Equipment Simulation Group, APRDL
3501 Ed Bluestein Boulevard, MD: K-10
Austin, TX 78721

Kevin Davis
Reaction Engineering International
77 West 200 South Suite 210
Salt Lake City, Utah 84101

Jeffrey J. Derby
Dept. of Chemical Eng. and Materials Science
University of Minnesota
421 Washington Ave. S.E.
Minneapolis, MN 55455

Yusheng Feng
Equipment Simulation Group, APRDL
3501 Ed Bluestein Boulevard, MD: K-10
Austin, TX 78721

J. E. Flaherty
Computer Science Dept.
Rensselaer Polytechnic Inst.
Troy, NY 12180

Paul Giguere
Group TSA-8
MS K575
Los Alamos National Laboratory
Los Alamos, NM 87545

R. J. Goldstein
Mechanical Engineering Department
University of Minnesota
111 Church St.
Minneapolis, MN 55455

R. Greif
Mechanical Engineering Department
6107 Etcheverry Hall
University of California
Berkeley, CA 94720-1740

Mike Heroux
Cray Research Park
655F Lone Oak Drive
Eagan, MN 55121

Dan Hitchcock
US Department of Energy
SCS, ER-30 GTN
Washington, DC 20585

Fred Howes
US Department of Energy
OSC, ER-30, GTN
Washington, DC 20585

Michael K. Jensen
Rensselaer Polytechnic Institute
Troy, NY 12180-3590

Klavs J. Jensen
Massachusetts Institute of Technology
Dept. Chem. Eng. MIT 66-566
Cambridge, Mass. 02139-4307

David Klipstein
Reaction Design
11436 Sorrento Valley Road
San Diego, CA 92121

T.J. Mountziaris
Department of Chemical Engineering
303 Furnas Hall
State University of New York
Buffalo, NY 14260-4200

S. V. Patankar
Mechanical Engineering Department
University of Minnesota
111 Church St.
Minneapolis, MN 55455

Todd Salamon
Rm. 7D-212
Lucent Technologies
600 Mountain Avenue
Murray Hill, NJ 07974

Jeffrey Scroggs
Department of Mathematics
North Carolina State University
Box 8205
Raleigh, NC 27695-8205

Farzin Shakib
ACUSIM SOFTWARE, INC.
14395 Saratoga Ave., Suite 120
Saratoga, CA 95070

T. W. Simon
Mechanical Engineering Department
University of Minnesota
111 Church St.
Minneapolis, MN 55455

Tyler Thompson
The Dow Chemical Company
External Technology / Cooperative Research
Building 1801
Midland, MI 48674-1801

Max Tirtowidjojo
DOW Chemical, Engineering Sciences
2301 N. Brazosport Blvd., B-1226
Frreport, TX 77541-3257

Dionisios Vlachos
Chemical Engineering Department
University of Massachusetts Amherst
159 Goessmann Lab, Box 33110
Amherst MA 01003-3110

David West
DOW Chemical, Engineering Sciences
2301 N. Brazosport Blvd., B-1226
Frreport, TX 77541-3257

Colin Wolden
Chemical Engineering and Pet. Ref. Department
Colorado School of Mines
P.O. Box 4028
Golden CO 80401-1887

INTERNAL DISTRIBUTION:

1	MS 0151	Gerold Yonas, 9000
1	MS 0321	William Camp, 9200
1	MS 0601	Jeff Tsao, 1126
10	MS 0601	Harry K. Moffat, 1126
1	MS 0601	M. E. Coltrin, 1126
1	MS 1111	Sudip Dosanjh, 9221
1	MS 1111	Scott Hutchinson, 9221
10	MS 1111	John N. Shadid, 9221
20	MS 1111	Andrew G. Salinger, 9221
1	MS 1111	Gary L. Hennigan, 9221
1	MS 1111	Rod C. Schmidt 9221
1	MS 1111	Matt St. John, 9921
1	MS 1111	Joe Castro, 9921
1	MS 1110	Ray S. Tuminaro, 9222
1	MS 1111	Karen Devine, 9226
1	MS 1111	Robert W. Leland, 9226
1	MS 0819	James S. Perry, 9231
1	MS 0819	Allem C. Robinson, 9231
1	MS 0841	P. L. Hommert, 9100
1	MS 0833	Johnny H. Biffle, 9103
1	MS 0316	E. D. Gorham, 9209
1	MS 0843	A. C. Ratzel, 9112
1	MS 0834	M. R. Baer, 9112
1	MS 0834	A. S. Geller, 9112
1	MS 0834	R. R. Torczynski, 9112
1	MS 0826	W. L. Hermina, 1553
1	MS 0826	T. J. Bartel, 9153
1	MS 0825	C. C. Wong, 9154
1	MS 0827	Randy Schunk, 9111
1	MS 0827	Phil Sackinger, 9111
1	MS 0827	Mario Martinez, 9111
1	MS 0827	Mike Glass, 9111
1	MS 0827	Polly Hopkins, 9111
1	MS 0827	Jim Schutt, 9111
1	MS 0827	Steve Kempka, 9111
1	MS 0834	Robert B. Campbell, 9112
1	MS 0835	Roy E. Hogan Jr., 9111
1	MS 0819	Mark A. Christon, 9231
1	MS 0826	Robert J. Cochran, 9114
1	MS 9042	Joseph F. Grcar, 8345
1	MS 9042	Chris Moen, 8345
1	MS 9042	Fran Rupley, 8345
1	MS 9042	S. K. Griffiths, 8345
1	MS 9042	Greg Evans, 8345
1	MS 9042	Bill Houf, 8345
1	MS 9042	Aili Ting, 8345
1	MS 9042	Ellen Meeks, 8345
1	MS 9042	W. Winters, 8345
1	MS 9051	Habib Najm, 8351
1	MS 9052	Mark Allendorf, 8361
1	MS 9018	Central Technical Files, 8940-2
5	MS 0899	Technical Library, 4916
2	MS 0619	Review & Approval Desk, 12690 For DOE/OSTI